HEP (2006) 175:23–57

Molecular Microfluorometry: Converting Arbitrary Fluorescence Units into Absolute Molecular Concentrations to Study Binding Kinetics and Stoichiometry in Transporters

J. W. Schwartz[1] · D. Piston[2] · L. J. DeFelice[3] (✉)

[1]Imaging Center, Stowers Institute for Medical Research, 1000 E 50th St., Kansas City MO, 64110, USA

[2]Department of Molecular Physiology and Biophysics, Department of Molecular Physiology and Biophysics, Vanderbilt University Medical Center, Nashville TN, 37232-8548, USA

[3]Department of Pharmacology, Center for Molecular Neuroscience, Vanderbilt University Medical Center, Nashville TN, 37232-8548, USA
lou.defelice@vanderbilt.edu

Abstract Cotransporters use energy stored in Na^+ or H^+ gradients to transport neurotransmitters or other substrates against their own gradient. Cotransport is rapid and efficient, and at synapses it helps terminate signaling. Cotransport in norepinephrine (NET), epinephrine (EpiT), dopamine (DAT), and serotonin (SERT) transporters couples downhill Na^+ flux to uphill transmitter flux. NETs, for example, attenuate signaling at adrenergic synapses by efficiently clearing NE from the synaptic cleft, thus preparing the synapse for the next signal. Transport inhibition with tricyclic antidepressants prolongs neurotransmitter presence in the synaptic cleft, potentially alleviating symptoms of depression. Transport inhibition with cocaine or amphetamine, which respectively block or replace normal transport, may result in hyperactivity. Little is known about the kinetic interactions of substrates or drugs with transporters, largely because the techniques that have been successful in discovering trans-

porter agonists and antagonists do not yield detailed kinetic information. Mechanistic data are for the most part restricted to global parameters, such as K_m and V_{max}, measured from large populations of transporter molecules averaged over thousands of cells. Three relatively new techniques used in transporter research are electrophysiology, amperometry, and microfluorometry. This review focuses on fluorescence-based methodologies, which—unlike any other technique—permit the simultaneous measurement of binding and transport. Microfluorometry provides unique insights into binding kinetics and transport mechanisms from a quantitative analysis of fluorescence data. Here we demonstrate how to quantify the number of bound substrate molecules, the number of transported substrate molecules, and the kinetics of substrate binding to individual transporters. Although we describe experiments on a specific neurotransmitter transporter, these methods are applicable to other membrane proteins.

Keywords Cotransporters · Neurotransmitters · Synapses · Membranes · Norepinephrine · Dopamine · Serotonin · Antidepressants · Cocaine · Amphetamine · Kinetics · Electrophysiology · Amperometry · Microfluorometry · Binding · Fluorescence · Stoichiometry

1 Introduction

1.1 Neurotransmitter Transporters Conduct Transmitters Across Membranes

Central nervous system (CNS) signaling relies on chemical transmission between adjacent neurons. After a stimulus-evoked response, the presynaptic neuron releases neurotransmitter (NT) into the synaptic cleft, activating pre- and postsynaptic ligand-gated channels or secondary messenger cascades (Fig. 1A and B). Chemical transmission is attenuated by NT degradation, diffusion, and clearance (Fig. 1C). The majority of transmitter molecules are sequestered in the presynaptic neuron via NT transporters (Axelrod and Kopin 1969; Graefe et al. 1978; Iversen et al. 1967). For example, the norepinephrine transporter (NET) removes 90% of released NE in peripheral noradrenergic neurons (Blakely 2001), and genetic NET ablation induces a significant increase in extracellular NE longevity (Moron et al. 2002; Wang et al. 1999; Xu et al. 2000). Serotonin (5-HT) and dopamine (DA) have similar transporters, SERT and DAT, respectively. Noradrenergic signaling disruptions have profound physiological effects because they influence attention, learning, memory, emotion, and pain reception (Foote and Aston-Jones 1995; Foote et al. 1980; Valentino et al. 1983). Furthermore, adrenergic dysfunction is associated with mood disorders such as depression (Clark and Russo 1998; Schildkraut et al. 1965) and posttraumatic stress disorder (Maes et al. 1999), hypertension, diabetes cardiomyopathy, and heart failure (Backs et al. 2001; Merlet et al. 1999).

The monoamine transporters, NET, SERT, and DAT are biological targets for drugs of abuse, such as cocaine and amphetamines, and tricyclic antidepressants (Ritz et al. 1990; Sacchetti et al. 1999; Tatsumi et al. 1997). NT transporter

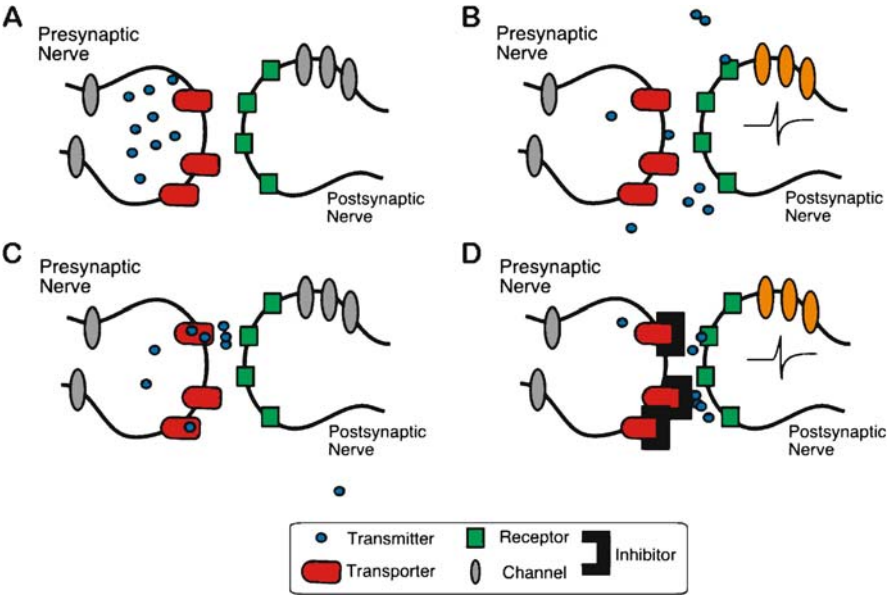

Fig. 1 A–D Neurotransmitter transporters regulate synaptic transmitter concentrations. Resting neurons have a reserved pool of docked synaptic vesicles primed for release (**A**). Electrical stimulation triggers transmitter release (**B**), which is subsequently sequestered into the presynaptic neuron (**C**). Transporter inhibition increases the synaptic cleft neurotransmitter longevity

inhibition delays NT clearance and thus increasing synaptic activity and altering the encoded information (Fig. 1D). In depressed patients, administration of antidepressants, such as Prozac (fluoxetine), alleviates the symptoms of depression via SERT inhibition. Drugs of abuse, such as cocaine, demonstrate more profound effects, which may be attributed to their nonselective nature. NET, SERT, and DAT are all inhibited by cocaine with similar potencies (Torres et al. 2003).

A single gene on chromosomes 5, 16, and 17 encodes DAT, NET, and SERT, respectively (Hahn and Blakely 2002). NET and SERT demonstrate alternative splicing, producing two distinct messages encoding NET and SERT (Bauman and Blakely 2002; Bradley and Blakely 1997; Kitayama et al. 1999, 2001). Both SERT messenger RNA (mRNA) messages maintain expression and function (Bradley and Blakely 1997). However, only one NET mRNA message is expressed and functions (Kitayama et al. 1999, 2001). The coexpression of the nonfunctional mutant with the functional NET protein dominantly inhibits NET activity, suggesting communication between gene products. To date, no DAT splice variants have been described. Due to the biological importance of transporter encoded by single genes, several genetics studies have focused on analysis of the coding sequence for single nucleotide polymorphisms. Pa-

tients with complex disorders were examined for monoamine transporter polymorphisms resulting in functional loss. For example, coding single nucleotide polymorphism (cSNPs) in human (h)NET are linked to orthostatic intolerance (OI). Patients suffering from OI demonstrate an increase in standing heart rate (<30 bpm) not accompanied by hypotension (Robertson et al. 2001; Shannon et al. 2000). A subset of OI patients with NE spillover and decreased NE clearance were examined for alterations in the NET gene. These studies reveal an OI-linked heterozygote G to C substitution at nucleotide 247 resulting in a proline substitution for alanine (Robertson et al. 2001; Shannon et al. 2000). In heterologous expression systems, this mutation retards expression and maturation and exhibits a dominant-negative NET inhibition (Hahn et al. 2003). DAT and SERT polymorphism linkage studies correlate with substance abuse/dependence, bipolar disorder, major depressive disorder, attention deficit/hyperactivity disorder and anxiety, unipolar depression, and suicidal patients. Genetic complex linkages are discussed in detail by Hahn and Blakely (2002).

NET, SERT, and DAT belong to the GAT1/NET Na/Cl-dependent NT transporter gene family (Blakely 1992). GAT1 transports the inhibitory NT, GABA (γ-aminobutyric acid). The Na/Cl-dependent, NT-transporter gene family is functionally defined by the millimolar Na^+- and Cl^--concentration dependence for substrate symport (Blakely 1992). The nomenclature for individual transporters is based on the specific neuronal subtype (noradrenergic, dopaminergic, etc.); thus, individual transporters are defined by the endogenous substrate. For example, NET accumulates NE in presynaptic noradrenergic neurons (Schroeter et al. 2000). Although the nomenclature implies selectivity, transporters demonstrate promiscuous substrate selection. 1-methyl-4-phenylpyridine (MPP^+) is a structurally distinct exogenous substrate that is a substrate for NET, SERT, and DAT (Scholze et al. 2002; Sitte et al. 1998, 2000, 2001). MPP^+ is the neurotoxic metabolite of 1-Methyl-4-phenyl-1,2,3,6-tetrahydropyridine, which after intravenous administration induces a DAT-dependent parkinsonian state within 2 weeks. Although monoamine transporters demonstrate selective substrate and inhibitor profiles, separate genes encode NET, SERT, and DAT. The predicted topology describes a 12 transmembrane domain (TMD) protein with an intracellular amino and carboxy termini, and this topology has become a hallmark of the Na^+/Cl^--dependent NT transporter gene family (Blakely 1992). NET and DAT demonstrate 80% amino acid conservation, and NET and SERT demonstrate 60% amino acid conservation (Blakely et al. 1991).

In order to study ionic dependence, radiometric substrate accumulation is traditionally monitored in media in which Na^+ and Cl^- are replaced: Na^+ is typically replaced with *N*-methyl-D-glucamine ($NMDG^+$) or Li^+ at equivalent osmolarity; however, these counter ions do not support substrate accumulation. A similar approach was employed to evaluate Cl^--dependent substrate accumulation. Unlike Na^+, Cl^- removal reduces but does not completely elimi-

nate substrate accumulation. Br^- and SCN^- (thiocyanate) substitution for Cl^- sustains a significant 5-HT SERT-mediated transport activity (~80%; Nelson and Rudnick 1981). Similar NET studies demonstrate that NET-mediated NE accumulation is Na^+ dependent, while Cl^- removal inhibits, but does not abolish, NE accumulation (Bonisch and Harder 1986; Corey et al. 1994; Harder and Bonisch 1985). These studies do not specifically address the ionic-dependent substrate binding. To evaluate the Na and Cl requirements for substrate binding, low-affinity substrate binding prohibits radiometric substrate binding measurements; thus, high-affinity antagonist displacement is used to approximate substrate affinity. Humphreys and coworkers measured [^{3}H]-imipramine and [^{125}I]-β-carbomethoxy-3β-(4-iodophenyl)tropane ([^{125}I]-β-CIT) in the Na-free and Cl-free experimentation; NaCl was replaced with LiCl and Na-isethionate, respectively. According to these data, [^{3}H]-imipramine binding was both Na^+ and Cl^- dependent, while [^{125}I]-β-CIT binding did not depend on Na^+ or Cl^-. 5-HT displaces bound [^{125}I]-β-CIT in Na^+-free and Cl^--free media, which indicates 5-HT interacts with SERT in the absence of Na^+ and Cl^-. Although Humphreys and coworkers argue Li^+ was inert, a recent study describes Li^+-induced conformation changes specific to Li^+ and no other alkali metals (Ni et al. 2001). Li^+ also produces an enhanced current in the absence of substrate (Ramsey and DeFelice 2002).

1.2 Methods to Study Transporter Function

Radiometric substrate accumulation, electrophysiology, and amperometry/cyclic voltammetry measure NET activity in different ways. Each method attempts to enhance one or more of the following criteria: (1) specificity, (2) rapid sampling, (3) dynamic substrate analysis, (4) amenability to single cells, and (5) segregation of substrate binding from substrate accumulation.

1.2.1 Radiometric Assay

In the classic radiometric assay, NET-expressing cells or resealed membrane vesicles are incubated with radiolabeled NE for approximately 5–10 min (shortest assay time is often about 30 s). The applied substrate is removed, and the cells or resealed vesicles are solubilized with detergent; the radioactive native substrate is measured by scintillation. The radiometric approach specifically monitors radiolabeled substrate; thus, it provides a high signal-to-noise ratio. The total number of cells is determined by a hemocytometer; thus, radiometric values provide a mean accumulation rate. The hemocytometer values, however, include dead cells, which reduce the reported accumulation values. Under these conditions, the accumulation rates are an underestimate. The radiometric approach has poor time resolution (>30 s) and cannot dynamically monitor

substrate accumulation; thus parallel samples are analyzed at increasing time points to measure transport rates. The maximal transport velocity (V_{max}) is determined by measuring transport rates with increasing substrate concentration until saturation. The theoretical components of maximal transport velocity are:

$$V_{max} = N\upsilon\nu \tag{1}$$

where N is the number (#) of functional transporters, υ is the number (#) of substrate molecules transported per transport cycle (per turnover), and ν is the turnover rate (1/s) of an individual transporter. However, the radiometric method does not directly measure individual transporter kinetics and depends on macroscopic measurements that are extrapolated to underlying molecular properties. The radiometric approach is also too insensitive to monitor single mammalian cells; for example HEK-293 cells—a typical cell line used in experiments—are approximately 10 μm in diameter with an approximate volume of 1.5 nl. These constraints render single-mammalian-cell radiometric assays infeasible; thus, radiometric assays typically employ thousands of cells and the condition of individual cells remains unknown. To get around this limitation, single-cell accumulation measurements have been made in *Xenopus* oocytes, which are approximately 1 mm in diameter and have a volume of 1 μl. Frog oocytes are also amenable to controlled conditions. However, some mRNA transcripts express poorly in oocytes; in particular, NET is a difficult transcript from which to recover active protein.

The classic radiometric approach measures net accumulated substrate, not substrate binding. A radiometric-binding assay exposes monoamine transporter-expressing cells or resealed vesicles to a radiolabeled ligand followed by vacuum filtration to remove excess ligand. Under these conditions, the substrate must remain bound long enough to filter the membranes, thus removing the unbound ligand. The corresponding ligand must remain bound for approximately 1 s. Monoamine transporter substrates do not remain bound for a sufficient time to separate unbound ligand by filtration methods. In order to estimate substrate binding, indirect methods are employed. High-affinity antagonists such as cocaine remain bound to monoamine transporter long enough to quantify, and agonist displacement of antagonist is used as an indirect measure of substrate potency. A radiometric high-affinity antagonist binding assay is employed to calculate the total number of surface monoamine transporters. Monoamine transporter-expressing cells or resealed vesicles are exposed to high-affinity antagonist concentrations. Eventually, all surface transporters are saturated providing the maximum number of bound antagonists (B_{max}).

$$B = \frac{B_{max}}{K_D^n + [L]^n} \tag{2}$$

B is the number (#) of bound ligands at each ligand concentration, B_{max} is the maximum concentration of bound ligands, K_D is a dissociation constant, L is the concentration of ligand exposed to the transporter, and n is the Hill coefficient. The radiometric approach reports the maximal number of inhibitor binding sites, not the monoamine transporter number, N, and not the number of functional transporters. To extrapolate transporter number N from B_{max}, the relative antagonist stoichiometry is assumed to be one ligand bound per functional transporter. These data are often compared to the maximal transport velocity (V_{max}) to establish an estimate of transport cycle (turnover).

$$V = \frac{V_{max}}{K_m^n + [S]^n} \tag{3}$$

V is the velocity at each substrate concentration, V_{max} is the maximum transport velocity, S is substrate concentration, K_m is the Michaelis-Menten constant, and n is the Hill coefficient.

1.2.2 Electrophysiology

Over 10 years ago, Bruns et al. performed a remarkable experiment. They measured SERT-mediated current in Retzius neurons dissociated from the leech and demonstrated a large (500–1000 pA), whole-cell, SERT-mediated currents that were induced by 5-HT application at a holding potential of −80 mV (Bruns et al. 1993). These presynaptic, SERT-mediated currents were sensitive to Na^+ and were inhibited by zimelidine, a specific SERT blocker; furthermore, they preceded the 5-HT-stimulated postsynaptic currents by several milliseconds. The SERT-mediated currents observed by Bruns and coworkers were later recapitulated in *Xenopus* oocytes expressing SERT and monitored with a two-electrode voltage clamp. The *Xenopus* oocyte expression system permits an assessment of the electric current profile in transfected and nontransfected oocytes; nontransfected oocytes do not accumulate 5-HT, nor do they demonstrate 5-HT-induced currents. Surprisingly, the presumably electroneutral SERT produced a large current carried predominately by Na^+ movement (Mager et al. 1994).

According to the classic fixed stoichiometry model of transport, ionic movement via NET produces the redistribution of a single positive charge, thus making the transporter electrogenic (Rudnick and Nelson 1978). Accordingly, HEK-293 cells stably expressing approximately $n = 10^6$ transporters/cell were expected to produce less than 0.2 pA of current, with all transporters working at the same time. When the experiment was performed, NET-mediated currents were 250-fold larger than the predicted value (∼50 pA, depending on membrane voltage). Thus, there are many more charges moving than substrate molecules. Furthermore, NET permits the movement of ions even in the absence of substrate, and NET inhibitors block this constitutive current.

The so-called "leak current"—charge movement without concurrent substrate movement—is revealed easily by the preemptive antagonist administration (Galli et al. 1995). Under whole-cell patch clamp conditions, cocaine administration to hNET-293 cells reduces the NE-induced whole-cell current. DAT electrophysiological profiles also demonstrate unexpectedly large charge movements and leak currents (Sonders et al. 1997). These experiments also describe the voltage-dependent uptake process in which DA accumulation increases with depolarization.

The unexpected substrate-induced currents prompted the determination of relative Na^+ and substrate contributions to the total charge movement (NE, DA, and 5-HT are monovalent cations). The ratio of charge movement to substrate transport (ρ) is an intrinsic transporter property that describes the channel contribution to transporter activity.

$$\rho = \frac{Number\ of\ Charges}{Number\ of\ Substrates} \tag{4}$$

In this equation, ρ measures the stoichiometry of transport. If $\rho = 1$, for example, that would mean one net charge per one NE-transported molecule through NET [in this case, the postulated NE:Na:Cl stoichiometry (Bonisch et al. 1986)]. Values of ρ greater than one are taken to imply an "uncoupled" current, although coupling per se is rarely measured. NET stoichiometry has been assessed using patch clamp and amperometry, yielding $\rho > 0$ (Galli et al. 1996). SERT and DAT have been assessed by concurrent two-electrode voltage clamp and radiolabeled substrate accumulation in frog oocytes. For DAT and SERT, transport velocity V (Eq. 3) increases linearly with hyperpolarization; however, the dependence of ρ on voltage was nonlinear. The maximal ρ values were obtained at −80 mV, with a minimum at 20 mV. Current traces were subsequently analyzed to determine the unitary charge movements associated with both current and transport. These analyses demonstrate that in *Drosophila* SERT ρ exceeds 100. Furthermore, roughly 500 5-HT molecules are translocated per channel opening (Petersen and DeFelice 1999).

The electrophysiological assays described above significantly improve the temporal resolution or transporter function, and they are amenable to single-cell analysis under voltage-controlled conditions. These experiments also provide new mechanistic information. The electrophysiological information, however, cannot provide the information on the species of the charge-carrying ions, and thus they are not as specific as the radiometric transport assay with regard to substrate identity. To alleviate this constraint, concurrent electrophysiological and amperometric approaches can be performed (Galli et al. 1996). These conditions permit identification of the substrate, single-cell assay, and voltage control, but they do not provide good time resolution and they cannot distinguish binding from transport.

1.2.3 Amperometry and Cyclic Voltammetry

NET does not express well in frog oocytes, thus methods used for DAT and SERT for the measurement of ρ cannot be used for NET. Using a series of voltage steps, NET coupling was assessed by concurrent current and amperometric measurements of NET activity in excised patches placed over a carbon fiber electrode. The potential across the carbon fiber is held constant at −700 mV, to oxidize NE. Under the assay conditions, NE is the only available oxidizable ion; thus, the oxidization is attributed to NE. NE oxidation produces two electrons that are subsequently recorded on an amperometric electrode. Due to the stochastic oxidation process, the current produced is directly proportional to the NE concentration exposed to the carbon fiber. Galli and coworkers have demonstrated ρ is directly proportional to voltage. These experimental data show that channel activity is coordinated to transport activity (Galli et al. 1998). These data show rapid NE movement through a patch (lower limit of 33,000 molecules/s; Galli et al. 1998).

The amperometric approach monitors NE from excised patch providing a similar single-cell measurement. Positioning the carbon fiber electrode under the patch pipette can permit the sampling of up to 95% of the total release transmitter (Galli et al. 1998). A carbon fiber electrode placed adjacent to a cell under whole-cell patch clamp conditions samples a subset of release molecules. The use of amperometry in combination with electrophysiology permits rapid sampling of the endogenous substrate, but this method is technically challenging. This combinational approach requires a researcher to pull an excise patch and move the electrode over the corresponding carbon fiber electrode. During the alignment process, the patch must remain intact, which requires delicate dexterity. By placing the patch electrode over the carbon fiber, the transport signal (amperometry) and current signal (patch electrode) are not synchronized. As transmitter exits the patch electrode, there is a delay prior to association with the carbon fiber. The chemical reaction on the carbon fiber adds another kinetic not accounted for in the analysis. The limitation reduced the time resolution for the concurrent amperometric and electrophysiological approach.

Another method proposed to measure substrate binding is cyclic voltammetry, in which a carbon fiber electrode is used to measure bath depletion of an oxidizable substrate. Mammalian cells or resealed vesicles expressing NET or DAT are incubated in a low bath volume with a sensitive electrode. Substrate oxidation is used to dynamically monitor the bath concentration. By examination, a reduction is the exposed concentration; the method extrapolates the internalized substrate concentration. Specific accumulation is defined in the presence of an inhibitor. In order to measure substrate binding, Schenk and coworkers measured DA depletion in Na^+-free conditions, and under these conditions the authors attribute a decrease in bath concentration to DA association with DAT (Batchelor and Schenk 1998; Earles and Schenk 1999; Povlock and Schenk 1997;

Schenk 2002; Wayment et al. 1998). The authors assume that in a Na-replaced media, the DA is only binding to the transporter without transport.

The radiometric, electrophysiological, and carbon-fiber approaches provide multiple methods to measure NET (and other transporters') activity. Each method has some desirable characteristic, whether it be specificity, rapid sampling, or applicability to a single, well-controlled cell. All of the described methods, however, fail to segregate binding and transport, nor do they permit spatially resolved signals with rapid sampling. Concurrent binding and transport measurements, for example, would allow researchers to distinguish functional transporters from plasma-membrane expression.

1.2.4 Quantitative Fluorescence Microscopy

Quantitative fluorescence microscopy offers a method to distinguish binding and transport, and it provides investigators with rapid sampling on single mammalian cells. The method also permits absolute signal quantification while segregating substrate binding and transport, thus allowing measurements of not only transport kinetic but also of substrate-transporter stoichiometry. Quantitative microscopy provides a single-cell, real-time, sub-micron, and simultaneous substrate binding and transport assay.

The methods to be described here calibrate arbitrary fluorescent units (AFUs) to the absolute number of molecules, and therefore to diffusion constants, enzyme kinetics, and photophysical properties. The following contains a brief description of confocal microscopy, two-photon excitation (TPE) microscopy, fluorescence lifetime imaging microscopy (FLIM), total internal reflection (TIRF) microscopy, fluorescence correlation spectroscopy (FCS), and fluorescence recover after photobleaching (FRAP). These methods have been employed to measure NET activity using a fluorescent surrogate substrate 1-4-(4-dimethylaminostyryl)-*N*-methylpyridinium (ASP^+) and green fluorescent protein (GFP) *N*-terminal tagged NETs. The fluorescent analog of MPP^+, ASP^+, is a neurotoxic metabolite of MPTP, and is a known substrate of monoamine transporters. Using ASP^+, we can assess binding and transport within 50 ms of application with submicron spatial resolution. For each photometric method, we outline the properties for each type of microscopy, along with its advantages and disadvantages.

These methods are employed to quantify fluorescent molecules. Fluorescence occurs when the ground state electrons are excited into a higher energy state via an interaction with a photon. To excite the ground state electrons, the excitation light energy must be at least equivalent to the energy gap between energy states. The energy dependence provides wavelength-dependent excitation, as energy is inversely proportional to wavelength. The excited-state molecule undergoes a series of internal energy conversions between higher energy states. The stored energy is rapidly dissipated by photon release. The emitted photon

has decreased energy, thus is emitted at a longer wavelength. Unfortunately, fluorescent molecules are eventually destroyed (i.e., photobleached) by continued excitation and emission, thus limiting the number of photons produced by a molecule. A typical fluorescent molecule, fluorescein, produces approximately 1 million photons prior to photodegradation (Pawley 1995).

Light, such as a fluorescence emission, can be measured with a photomultiplier tube (PMT). A PMT possesses a photoactive surface producing electrons when exposed to light. The resultant electron is magnified through a series of electron-sensitive surfaces that cascade and amplify each incident photon. The PMT signal is directly proportional, over a linear range, to the number of photons striking the photoactive surface; some PMTS are sensitive enough to measure a single photon. The absorbed photons are thus translated into an electrical signal. Another device used to measure light is a charge-coupled device (CCD), which also uses a photoactivated surface to convert the number of photons into an electrical signal. The photoactive surface is divided into subregions and the photons absorbed within each subregion are independently quantified. A computer creates a digital image by registering each sub region. A CCD is a central component in most digital cameras. Although CCDs are often less sensitive than PMT-based detection, typical biological samples provide enough light to trigger a response on CCDs. In general, PMTs and CCDs provide adequate sensitivity for most biological samples.

Noise in a PMT- or CCD-based detection system comprises thermal noise, also known as dark current, readout noise, and shot noise. Thermal noise results from spontaneous PMT or CCD events that occur in the absence of light. The photoactive surface will spontaneously emit electrons, triggering a nonspecific cascade. Thermal noise is reduced by cooling the light recording device, which is a common method used in cooled-CCD cameras. Readout noise affects CCD cameras and can be reduced by slowing down the speed of the camera output. Shot noise is an intrinsic source of noise associated with the photon flux onto the PMT or CCD. A fluorescent molecule produces a stream of photons that excite the photoactive surface of the PMT. Although the average photon flux is constant, the instantaneous signal fluctuates around the mean. Poisson statistics mandate that the deviations are equivalent to the square root of the average number of photons. For example, a molecule producing an average photon count of 100 photons per unit time is accurate within a range from 90 to 110 photons $\left(\text{number of photons} \pm \sqrt{number\ of\ photons}\right)$. To reduce shot noise, the integration times are increased.

1.2.5 Confocal Microscopy and Two-Photon Excitation

Marvin Minsky developed the theory for confocal microscopy in 1957 (Minsky 1957). Confocal microscopy differs from wide-field (conventional) microscopy, permitting acquisition of optical slices of thick samples. Fluorescent specimens

are commonly visualized with epi-illumination, in which filtered excitation light is reflected by a dichroic mirror through an objective lens onto the sample. The emitted light, at a lower wavelength, is collected by the same objective lens and transmitted through the dichroic mirror to the detection surface. A confocal microscope inserts pinholes between both the excitation source and emission detector to reject out-of-focus light. Using the original Minsky design, an image is generated by rastering the stage, providing a complete image (Pawley 1995). The stage raster was a major challenge to producing commercial confocal microscopes. A laser excitation source provides high-intensity monochromatic light that does not require an excitation pinhole. Laser scanning confocal microscopy (LSCM) scans the optical field with *xy* scanning mirrors that move the laser beam across the field. At each point, the light is collected on a PMT and transformed to a digital image by a computer. Adjusting the focus generates optical slices, and the corresponding optical planes are digitally combined to generate a volume. The confocal point spread function (PSF) is estimated by a three-dimensional Gaussian function (Rigler et al. 1993), and the shape and size depend on the objective numerical aperture, wavelength of light, and size of the excitation beam (beam waist) (Rigler et al. 1993).

$$\overline{PSF}_{Confocal}(x, y, z) = \exp\left[-\frac{2(x^2 + y^2)}{\omega_o} - \frac{2z^2}{z_o^2}\right] \tag{5}$$

The PSF describes the volume encompassed by the single point using confocal microscopy, where ω_0 is the beam waist in the lateral direction and Z_o is the beam waist in the *z*-axial direction (Rigler et al. 1993). For example, a 1.4-numerical aperture (NA) 63 × oil immersion objective with a pinhole at 1.5 airy units (airy units are a normalized optical units, one airy unit equals the full width $1/e^2$ maximum for the first dark ring for the Airy diffraction pattern) produces an approximate volume of 0.30 fl. A complete description of confocal microscopy, including the calculation of the PSF and airy units, can be found in *Handbook of Biological Confocal Microscopy*, edited by James B. Pawley (Pawley 1995).

As described above, the thin segments generated by a confocal microscope are advantageous, but they are not a solution to all imaging problems. A detector for a confocal microscope is usually a PMT, which is limited by shot noise. The small volume generated under confocal microscopy limits the number of fluorescent molecules being sampled, thus reducing the number of photons being collected. In order to reduce noise, the integration time for each focal volume is increased, which increases the acquisition time. To reduce acquisition time, samples can be excited with more intense light, which expedites the photodegradation of the fluorescent molecule. The balance of acquisition time, pixel integration, and photobleaching can limit the time utility of confocal microscopy.

Confocal microscopy illuminates the entire sample, but acquires light emanating only from a small volume, typically roughly 0.15 fl. Fluorescent molecules outside the focal volume are simultaneously photobleached; therefore, the potential fluorescent signal decreases throughout the entire sample. As a sample is optically sliced, the later slices have a decreased signal due to prolonged exposure, thus limiting the penetration depth of confocal microscopy. TPE provides a solution to photobleaching outside the plane of focus. Using TPE, the excitation volume is limited by the photon density. Normally, a fluorescent molecule is excited by a single photon, but simultaneous absorption of two photons at half the energy (double the wavelength) can produce photoexcitation. TPE requires nearly simultaneous absorption of two photons. The probability of two photons being simultaneously absorbed increases in the focal volume, which has a higher photon density. The limited excitation area reduces out-of-plane photobleach.

In general, the TPE excitation wavelength is double the single-photon excitation wavelength, but the TPE excitation spectra can deviate from the doubling paradigm (Dickinson et al. 2003). The photon density is only sufficient to excite a fluorescent molecule within a small volume (Piston et al. 1995; Williams et al. 1994). The PSF for TPE can be well approximated by a Gaussian–Lorentzian function (Berland et al. 1995), and also depends on objective NA, wavelength, and beam waist.

$$\overline{PSF}_{TPE}(\rho, z) = \frac{4\omega_o^4}{\pi^2\omega^4(z)} \exp\left[\frac{-4\rho}{\omega^2(z)}\right] \; ; \quad \omega^2(z) = \omega_o^2\left(1 + \frac{z\lambda}{\pi\omega_o^2}\right) \tag{6}$$

The Gaussian–Lorentzian PSF describes the volume encompassed by the single point using TPE microscopy, where ω_0 is the beam waist in the lateral direction (Berland et al. 1995). By scanning the laser beam in the x–y direction and moving the objective focus, TPE generates a three-dimensional representation of the object. The volume difference for the wide-field PSF compared to confocal and TPE is significant, but at matched wavelengths with a small pinhole (<1 airy unit) the PSF for confocal microscopy and TPE (Berland et al. 1995) are similar; therefore, under wavelength-matched conditions, TPE does not enhance z-axial resolution compared to confocal microscopy.

TPE has several advantages over confocal microscopy: (1) reduced total sample photobleaching, (2) increased number of photons detected, and (3) enhanced tissue penetration. Due to the spatially constrained fluorescence, an emission pinhole is not necessary. Detectors can be positioned to collect all the light produced by the fluorescent event, significantly increasing the total number of photons sampled and reducing shot noise. The increase in collected photons reduces the integration time required to obtain photon counts, thus reducing the image acquisition time. The spatial constraints prohibit photobleaching the sample outside the excitation volume; thus, as a thick sample is optically sliced, the later slices have not been photobleached. The sustained signal into later planes enhances penetration depth. TPE uses infrared (IR)

radiation, which is not readily absorbed by biological samples. TPE is able to penetrate deeper into tissues, because IR radiation is not readily absorbed by tissue. Confocal microscopy often employs ultraviolet or visible excitation wavelengths, which are absorbed by endogenously expressed compounds within tissue. These same molecules do not absorb IR radiation. The enhanced penetration depth and reduction in out-of-plane photobleaching is advantageous for thicker samples (>200 μm).

Confocal microscopy permits optical isolation of subvolumes within thick samples, which is ideal for measuring ASP^+ binding separate from accumulation. By reducing the sample volume, the relative solution contribution to the total signal is negligible, while the cellular contribution remains high. NTs, amphetamines, and neurotoxins bind before being transported, whereas cocaine and antidepressants bind to block the substrate transport s. Although binding is crucial to transport, few assays separate direct effects on binding from effects on transport after binding, nor do they provide adequate temporal or spatial resolution to describe real-time kinetics or localize sites of active uptake. Monitoring changes in ASP^+ fluorescence, fluorescence microscopy distinguishes substrate binding from substrate transport using single-cell, space-resolved, real-time fluorescence microscopy. ASP^+ has micromolar potency for NET (Schwartz et al. 2003). The plasma membrane is visualized by acquiring concurrent differential interference contrast (DIC) images (Fig. 2A). After ASP^+ exposure, the plasma membrane of cells expressing NET demonstrates an immediate increase in ASP^+ fluorescence (Fig. 2B). Prolonged exposure permits cytosolic ASP^+ accumulation (Fig. 2C). Subsequent desipramine (DS) (a selective NET antagonist) displaces bound ASP^+ and inhibits further accumulation (Fig. 2D). Accumulated ASP^+ remains constant after DS administration; the increase in sequestered ASP^+ is parallel to the increase in mitochondrial ASP^+ accumulation (Schwartz et al. 2003). ASP^+ accumulation is Na^+-, Cl^--, cocaine-, and DS-sensitive, and temperature-dependent, and it competes with NE uptake. Monitoring ASP^+ with confocal microscopy provides a single-cell, rapid-sampling binding and transport assay for NET activity.

To evaluate NET surface distribution, we utilized confocal three-dimensional reconstruction to localize GFP-hNET and ASP^+ molecules. The N-terminal GFP-tagged NET (GFP-hNET) maintained 100% wildtype activity and bind ASP^+ with similar affinity. To evaluate the relative surface expression, we reconstructed the corresponding isosurface for HEK-GFP-hNET cells. Setting a threshold value to one AFU does not permit any gaps within the isosurface; this setting outlines the plasma membrane (Fig. 3a–C). Using a threshold value at the beginning of the dynamic range for the GFP signal (threshold = 64), the corresponding isosurface represents the distribution of colocalized GFP-hNETs and ASP^+ molecules. The GFP-hNET completely colocalizes with ASP^+ molecules. Colocalized GFP-hNET and ASP^+ are represented in yellow, and ASP^+ molecules alone are represented by red (Fig. 3d–F). By removing the

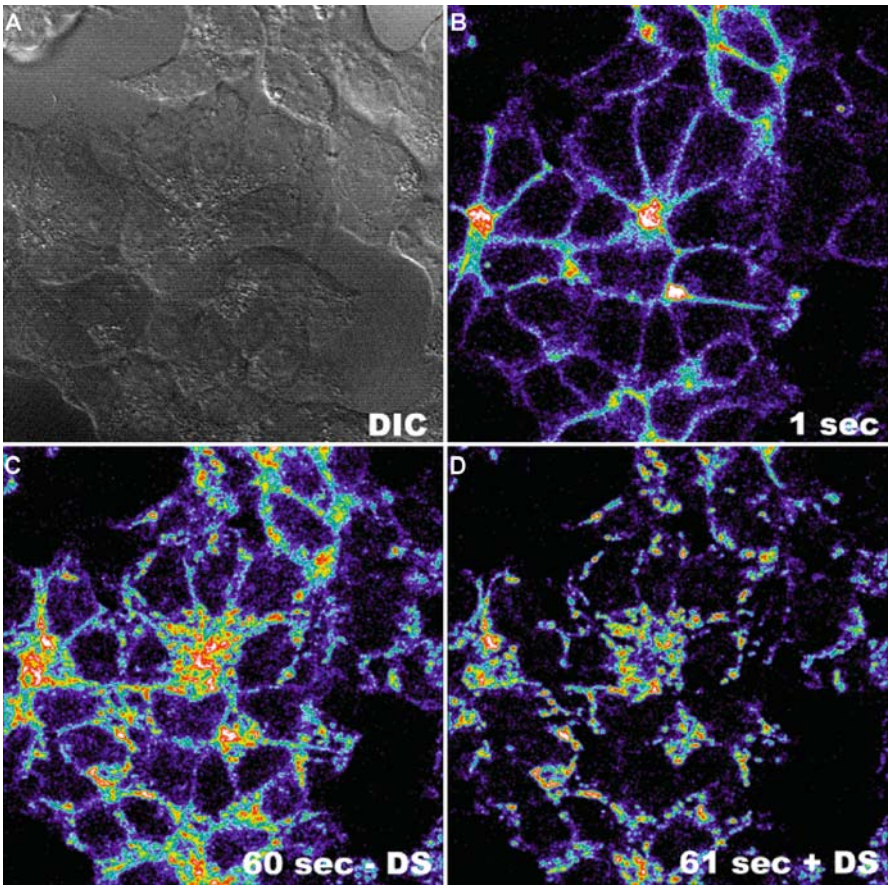

Fig. 2 A–D Desipramine displaces bound ASP^+. **A** The DIC image for HEK-293 cells expressing NET. A fluorescence image is acquired 1 s after ASP^+ exposure (**B**). The cells continue to incubate for 60 s (an image is recorded every 3 s). The 60-s image (**C**) is recorded prior to the addition of 10 μM desipramine. The next image recorded (3 s later, 63-s image) shows the displacement of bound ASP^+ (**D**)

last three optical sections (3 μm of GFP-hNETs), the underlying mitochondria are exposed (Fig. 3G–I). These data provide transporter localization and demonstrate that transporters are confined to subcellular regions across the cell surface. We further demonstrated that ASP^+ interacts with transporters not only in transfected cells but also in cultured neurons. As seen in Fig. 4, active NET is also localized to subcellular regions along superior cervical ganglia neurons. Because NET transport depends on internal substrate concentration, NET localization to pseudopodia, for example, may generate higher concentrations compared to other regions of the neuron. Thus, cellular localization may profoundly affect the accumulation rate. Indeed, the thin-filament pseudopo-

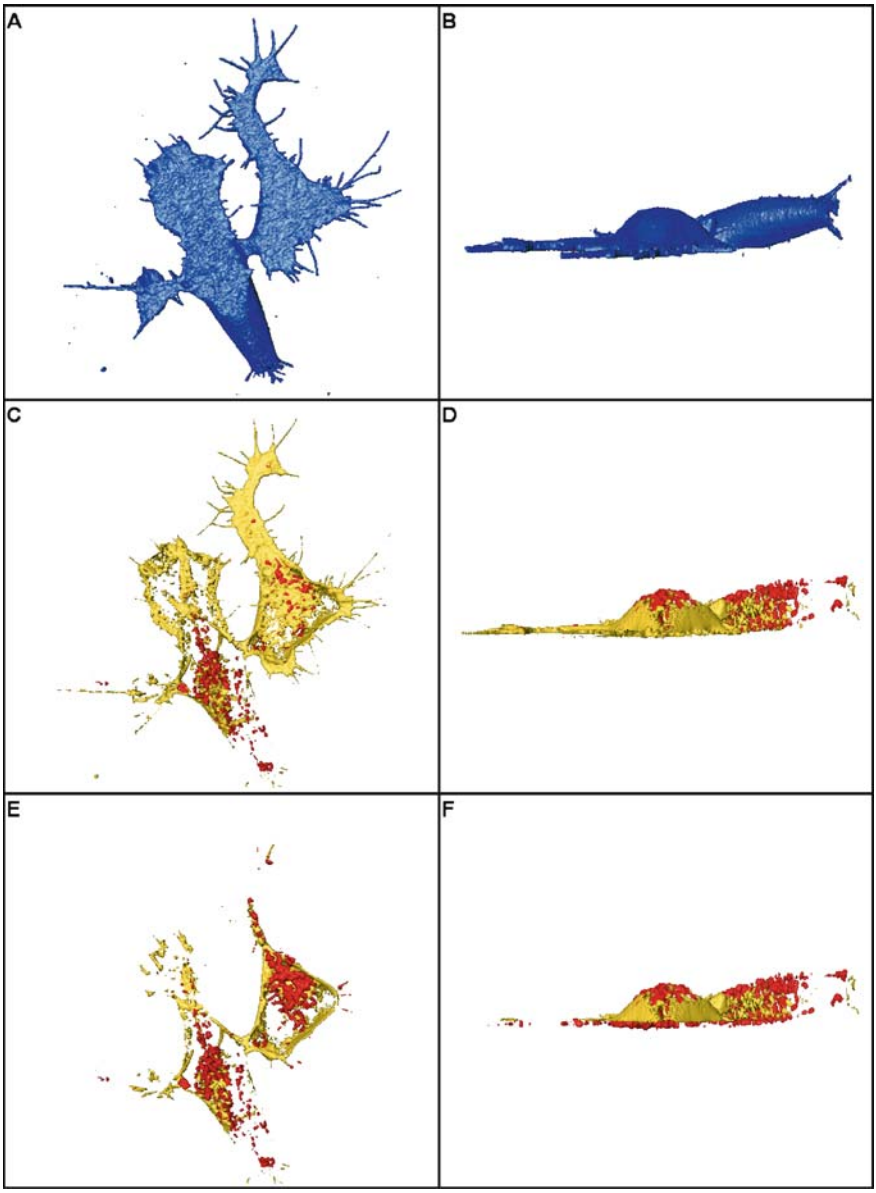

Fig. 3 A–F Isosurface GFP-hNET and ASP^+ surface distribution. All isosurface images were generated using Amira image analysis software. Each *column* represents and identical view angle for individual isosurfaces. **A**, **B** An isosurface of a single GFP-hNET cell. Isosurface was generated without permitting gaps within the isosurface. **C**, **D** The *yellow* isosurface represents colocalized GFP-hNET and ASP^+, while the *red* isosurface represents only ASP^+. **E**, **F** *Yellow* represents the GFP-hNET/ASP^+ isosurface, except the bottom three planes have been removed exposing the underlying mitochondria. QuickTime virtual reality (VR) files for each surface are published on the physical biology online version

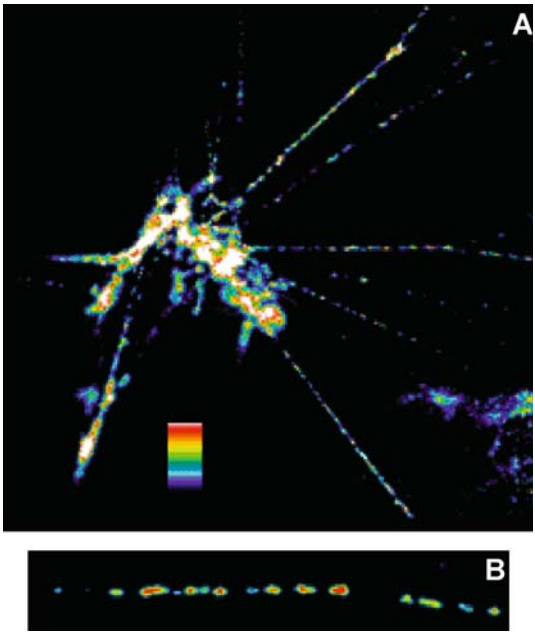

Fig. 4 A,B ASP^+ accumulates in superior cervical ganglia (SCG) neurons. **A** ASP^+ accumulation in SCG recorded after 60 s. ASP^+ accumulation is desipramine-sensitive. **B** A neurite at higher magnification. The *color gradient* represented in *panel a* denotes the color range corresponding to the intensity values

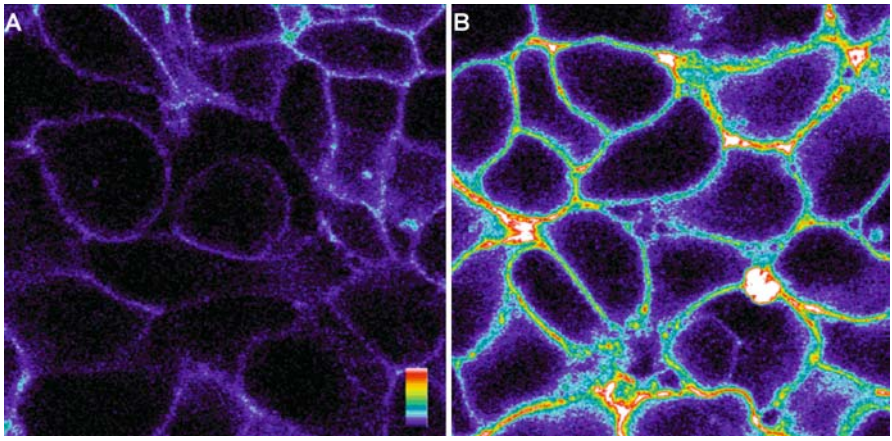

Fig. 5 A–C Cl^- replacement increases cell plasma membrane localized ASP^+ binding. **A** hNET-293 cells exposed to 2 μM ASP^+ for 1 s in KRH buffer. **B** HNET-293 cells exposed to 2 μM ASP^+ for 1 s in KRH buffer with 120 mM NaI replacing NaCl; 100 μM Cl^- present.

dia may represent the endogenous environment. In superior cervical ganglia neurons, NET localizes to small varicosities along the neurites (Fig. 4; see Schwartz et al. 2003). The transporter has a distinct substrate conductance, which is concentration-dependent. The varicosities may represent a diffusion barrier, thus significantly decreasing the volume the transporter is using for a concentration gradient.

Although transport *ex more* depends on Na^+ and Cl^-, binding is actually independent of Na^+ and increases in low Cl^-, while transport per se depends critically on Na^+ but is much less affected by Cl^-. In KRH media containing 120 mM NaCl, ASP^+ addition to HNET-293 cells causes an immediate increase in membrane-localized fluorescence (Fig. 5A, 1 s ASP^+ exposure). In order to evaluate ASP^+-binding ionic dependence, we exposed hNET-293 cells to KRH buffer in which Cl^- was replaced with I^-. Under these conditions, we observe a significant increase in bound ASP^+ (Fig. 5B, 1 s ASP^+). The increase in ASP^+ response is localized to the membrane and represents a twofold increase in plasma membrane ASP^+ fluorescence. These data indicate that more ASP^+ is binding to the cell surface, but does not address NET surface expression.

1.2.6 TIRF Microscopy

To evaluate NET surface expression, we employed TIRF microscopy using specialized optics to generate an evanescent wave with sufficient intensity to excite fluorescent molecules less than 1,000 Å from the coverslip. This thin optical section is ideally suited to measure areas juxtaposed to the coverslip. Using high NA oil immersion lenses (>1.45 NA) or a trapezoidal prism, a laser is adjusted at an angle of incidence greater than the critical angle for total internal reflection (Axelrod 1989, 2001a, b, 2003; Axelrod et al. 1983). At this angle, the change in refractive index between the sample index ($n = 1.33$) and coverslip ($n = 1.52$) completely reflects the incident light. The measured power of the light entering the objective and the corresponding reflected light are equivalent, if no molecules are present to absorb the photons within the evanescent field. TIRF illumination generates an electromagnetic field (called an "evanescent wave") which prorogates from the interface into the sample. Photons tunnel to excite a fluorescent molecule via evanescent field coupling. The field intensity decreases exponentially in the sample, and the intensity is only sufficient to excite molecules for the first 1,000 Å. This optical configuration permits exclusive membrane visualization with a significant enhancement in *z*-axial resolution compared to confocal or two-photon optical slices. The major disadvantage to TIRF imaging is that the area of interest within the sample must be adjacent to the coverslip. The exponential decay in intensity from the coverslip hinders but does not eliminate the ability to perform quantitative microcopy (Axelrod 2001b, 2003).

As shown above in Fig. 4, ASP^+ binding is enhanced twofold by Cl^- substitution with I. This increase may be attributed to a rapid increase in surface expression due to Cl^- removal. To evaluate this hypothesis, we used TIRF microscopy. Under these conditions, we exclusively examined GFP-hNET proteins localized to the membrane in the presence and absence of Cl^-. All surface NETs were occupied by ASP^+ under normal (120 mM NaCl) conditions. As seen in the TIRF images, the ASP^+ and GFP-hNET molecules form a pattern based on cell contact. Previous studies demonstrated that 2 μM ASP^+ occupies all surface transporters. According to the TIRF studies (Fig. 6), we observe identical GFP-hNET and ASP^+ distributions. Images collected before

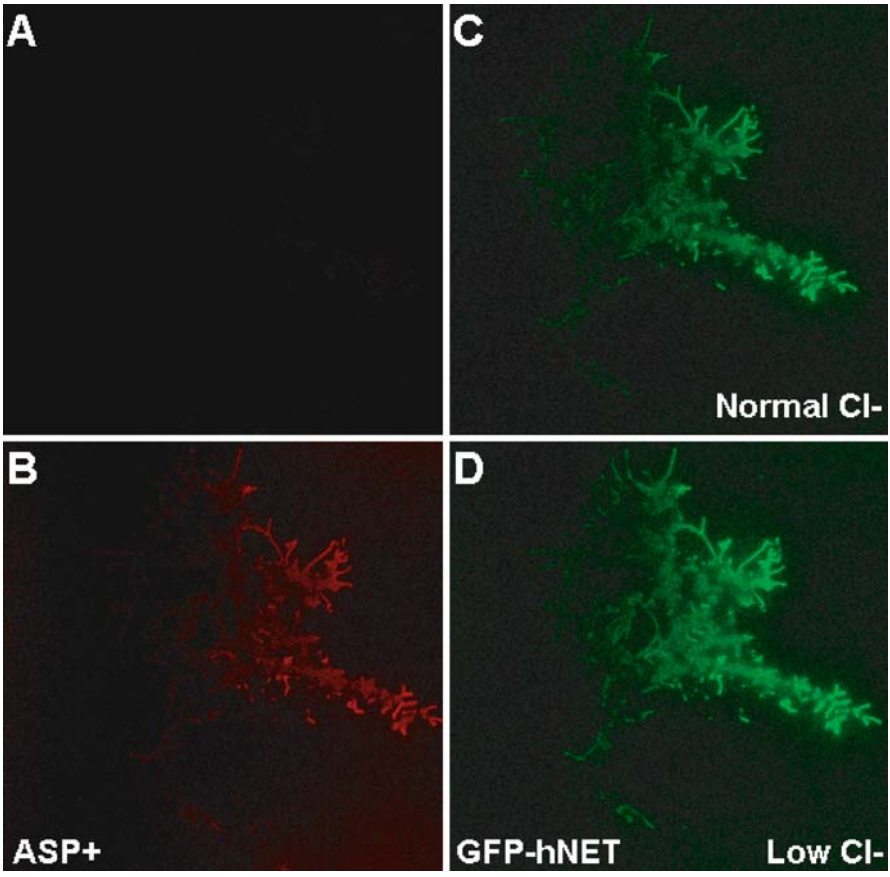

Fig. 6 A–D Cl^- removal does not elevate GFP-hNET distribution. Prior to 2 μM ASP^+ addition, GFP fluorescence is not recorded in the ASP^+ channel (**A**). Decreasing Cl^- concentrations does not elevate the GFP-hNET membrane distribution in normal, 120 mM, NaCl KRH buffer (**B**). The relative GFP-hNET transporter density does not change upon simultaneous 2 μM ASP^+ addition (**C**) in reduced Cl^- media (Cl^-<3 mM) (**D**)

ASP^+ addition indicate that GFP-hNET fluorescence does not appear in the ASP^+ channel (Fig. 6A, B). After 10 s of 2 μM ASP^+ exposure in Cl^--free media (NaI substation, FC Cl < 3 mM) hNET surface distribution is unaltered. These measurements provided a relative increase in substrate concentration. More extensive experimentation is required to address an absolute substrate concentration.

1.2.7 Fluorescence Lifetime Imaging Microscopy

FLIM provides information about the localized environment, permitting the calibration of confocal images. Fluorescence intensity measurements from a cellular context are not always sufficient to determine the fluorescent molecule concentration. Fluorescence intensity depends on the excitation light intensity (I_o), molar absorptivity (ε), the concentration ([c]), volume (L), and the quantum yield. The molar absorptivity, the ability to accept a photon at a defined wavelength, is largely independent on the localized environment (Lakowicz 1999). However, fluorescence is highly sensitive to the local environment, which leads to changes in quantum yield (Lakowicz 1999).

$$F = I_o \varepsilon [c] L Q_f \tag{7}$$

Fluorescence intensity is equivalent to the product of I_o, the excitation light intensity, ε, molar absorptivity, [c], fluorescent molecule concentration and Q_f, the quantum fluorescence quantum yield (Herman 2001). FLIM provides a concentration-independent measurement to evaluate environmental effects on a fluorescent molecule (Lakowicz 1999). Fluorescence lifetime measures the average time a population of molecules spends in the excited state. After excitation, a fluorescent molecule dissipates stored energy primarily as photons. In the absence of all other energy-releasing processes, the decay of photons from the excited state is defined as the natural decay of the molecule. Fluorescent molecules also dissipate energy via nonradiative mechanisms such as vibrational coupling. The combination of radiative and nonradiative processes results in the measured lifetime (Eq. 8), which can be defined in terms of the number of excited molecules (F_o) and the exponential decay constant.

$$F = F_o e^{-\frac{t}{\tau}} \tag{8}$$

F_o represents the number of molecules in the excited state and τ is the fluorescence lifetime (Lakowicz 1999). The quantum yield of fluorescence is proportional to the measured fluorescence decay divided by the natural fluorescence decay (Herman 2001).

$$Q_f = \frac{\tau_{measured}}{\tau_{natural}} \tag{9}$$

Q_f is the quantum yield for a fluorescence molecule. $\tau_{measured}$ is the measured lifetime. $\tau_{natural}$ is the fluorescence lifetime in the absence of all other energy releasing processes (Herman 2001). By substituting Eq. 5 into Eq. 1, fluorescence quantum yield changes between two local environments—such as solution and cellular—can be evaluated. A calibration curve in a solution can thus be calibrated to predict molecular concentration in the cell.

Fluorescence lifetimes are established using either frequency-domain (Fig. 7) or time-domain measurements (Fig. 8). Hanson and coworkers describe in detail the construction of a laser scanning FLIM microscope using frequency domain measurements (Hanson et al. 2002). Briefly, an appropriate TPE source, such as a titanium:sapphire laser (Millinia-pumped Tsunami, Spectra-physics), is coupled to the epi-fluorescence port of an inverted microscope. TPE excitation permits frequencies at 80 MHz; the corresponding TPE frequency must be similar to the fluorescent lifetime. The resultant fluorescence is recorded by a PMT and the sample scanned using an *xy* scanning mirror. A small portion of the excitation beam is diverted and recorded on a reference PMT. The phase and modulation of the high-frequency fluorescence emission are detected relative to the phase and modulation of the high-frequency repetitive light source. The fluorescence lifetime is calculated using the heterodyne frequency modulation method described by Jameson and coworkers (Alcala et al. 1985; Gratton et al. 1984; Jameson et al. 1984). Measuring a sample of known lifetime accounts for the microscope response, and all lifetime changes are additive. Alternatively, the fluorescence lifetime can be established by measuring the fluorescence

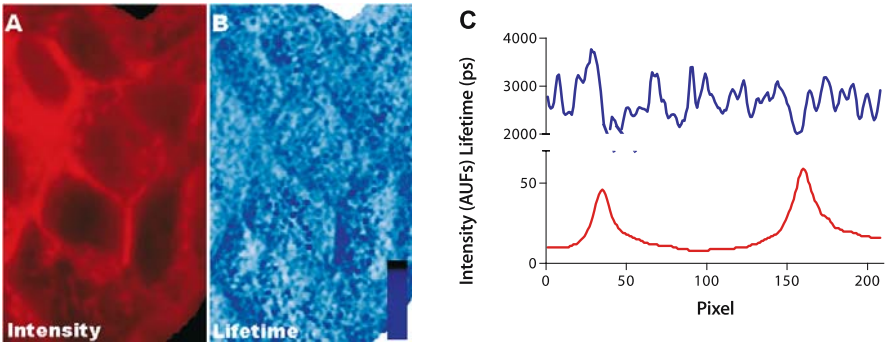

Fig. 7 A,B Frequency domain lifetime measurements. hNET-293 cells are exposed to 2 μM ASP^+ for 5 min prior to image acquisition. The changes in fluorescence intensity (**A**) and fluorescence lifetime (**B**) were examined using fluorescence lifetime imaging microscopy (FLIM) (see Sect. 1.2). The *color gradient* in *panel b* indicates the fluorescence lifetime value with *black* as the longest lifetime. Using the identical imaging settings, increasing concentrations of ASP^+ in isobutyl alcohol and GFP in water were imaged (*right panel*). The average pixel intensity across an image plan 10 μm from the coverslip was plotted against concentration [average ± standard error of mean (SEM), $n = 3$ ASP^+ slope = 26.5 AFU/μM, GFP slope = 15.3 ± 0.41 AFU/μM]. **C** Line scan

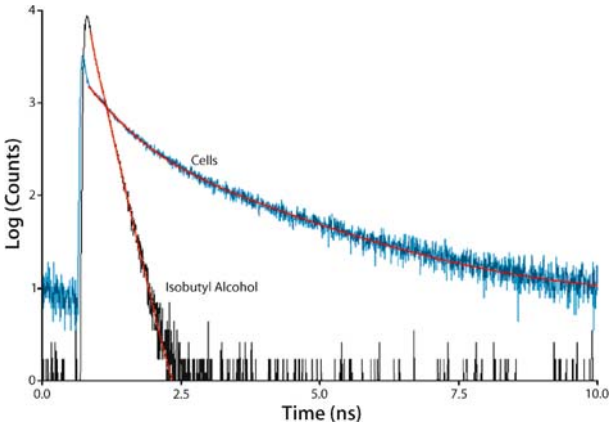

Fig. 8 Time-resolved fluorescence decay measurements establish the fluorescence lifetime. The cellular ASP^+ fluorescence lifetime was quantified using time-resolved fluorescence spectroscopy. The ASP^+ lifetime in the calibration solvent, isobutyl alcohol, and cellular lifetime was measured in a lifetime spectrometer. Cellular lifetime was measured by preloading hNET-293 cells with 5 μM ASP^+ for 10 min prior to harvest and washing. The log value for the photon counts is plotted against time, and the data are fit to the multi-exponential function $\left(Counts = A + Be^{-t/\tau} + Ce^{-t/\tau} + De^{-t/\tau}\ldots\right)$

decay in the time domain. A single focal spot is excited with a femtosecond laser pulse and the resultant fluorescence is recorded on a PMT. The decay is a measure of the fluorescence lifetime. Lifetime spectrometers and some microscopes utilize time-resolved fluorescence lifetime measurements.

FLIM has a few disadvantages. Currently, commercial FLIM systems are not readily available, and FLIM images have a slow acquisition rate. Several data points must be collected for each pixel in order to calculate the corresponding fluorescence lifetime. Multiple data point acquisition significantly delays image acquisition. A lifetime image can require as much as 6 min to obtain a single plane of an HEK-293 cell. To alleviate this constraint, single-pixel measurements at differing cellular locations are often sampled instead of acquiring data over an entire image.

Using FLIM, we measured the fluorescence lifetime of cellular ASP^+, which was significantly longer than ASP^+ in aqueous buffer. A fluorescence intensity image (Fig. 7A) was acquired concurrently with a fluorescence lifetime image (Fig. 7B). As seen in Fig. 7, for each pixel within the intensity image the corresponding fluorescence lifetime was determined. The solution ASP^+ fluorescence lifetime was significantly shorter (<10 ps) compared to cellular ASP^+ fluorescence lifetime (∼2.5 ns). GFP has the same quantum efficiency as aqueous buffer and the cytosol; thus, no lifetime changes were observed. A solution calibration is directly applicable to cellular GFP. Similar values were determined from corresponding time-domain measurements (Fig. 8). The time-domain measurements demonstrate a multi-exponential decay, which

shows that ASP^+ decays from several excited states. This is also reflected in frequency domain measurements, as τ_{phase} and τ_{mod} provided different fluorescence lifetime measurements.

In isobutyl alcohol, ASP^+ has an average lifetime of 168 ps, compared to 1,200 ps for cellular ASP^+. Therefore, a sevenfold increase was used to convert measured cellular fluorescence to absolute ASP^+ concentration values. Calibration curves for ASP^+ and GFP were examined at identical microscopy configurations. Confocal images of ASP^+ in isobutyl alcohol and GFP in water were acquired and the pixel histogram peak was plotted against concentration. GFP fluorescence is relatively independent of the local environment, thus lifetime corrections similar to those for ASP^+ were not required for GFP (Patterson et al. 1997). To avoid day-to-day variation, the microscope was calibrated daily. N-terminal GFP tagged hNET (GFP-hNET) maintains full transport activity. We collected dual channel ASP^+ and GFP-hNET time series using the calibrated settings. Under the conditions used, crosstalk between the GFP-hNET channel and ASP^+ channel was negligible. We converted pixel intensity to molecular values and the corresponding images for ASP^+ and GFP-hNET were compared. Panel a shows an overlay image taken at 10 s, and the yellow cell borders signify ASP^+ and GFP-hNET colocalization. Dividing a GFP-hNET image by the ASP^+ provided the GFP/ASP^+ ratio images. In the cell interior, the colocalization ratio approaches zero. Although the GFP-hNET and ASP^+ intensity varies along the cell perimeter, the ratio value is approximately constant and time-independent. Measuring the maximum number of GFP-hNET and ASP^+ molecules along a four-pixel-wide line scan along the cell circumference established the GFP-hNET to ASP^+ ratio. These data are summed over time for each cell ($n = 250$). The distribution ratio peaks at one GFP-hNET molecule per ASP^+ molecule; that is, one substrate associates with each hNET protein.

1.2.8 Fluorescence Correlation Spectroscopy

Another means to determine the underlying number of fluorescent molecules is FCS. FCS is a method where fluorescence from a single focal volume is measured over time, and small fluctuations in this signal provide information related to the number of particles, diffusion times, or enzyme kinetics. Over 30 years ago, Madge, Elson, and Webb (Elson et al. 1974; Magde et al. 1972, 1974) developed FCS to examine intercalated fluorescent particles in DNA. In FCS, small changes in the fluorescent signal arise due to an alteration in fluorescent molecule particle concentration from diffusion through the optical volume, enzymatic cleavage, or environmental changes (Fig. 9). In a simple case, as molecules enter the optical volume the fluorescence signal proportionally increases, but as molecules exit the optical volume the fluorescence signal proportionally decreases. Diffusion is only one of many processes that affect fluorescence. For example, after continued excitation, fluorescence molecules enter a dark

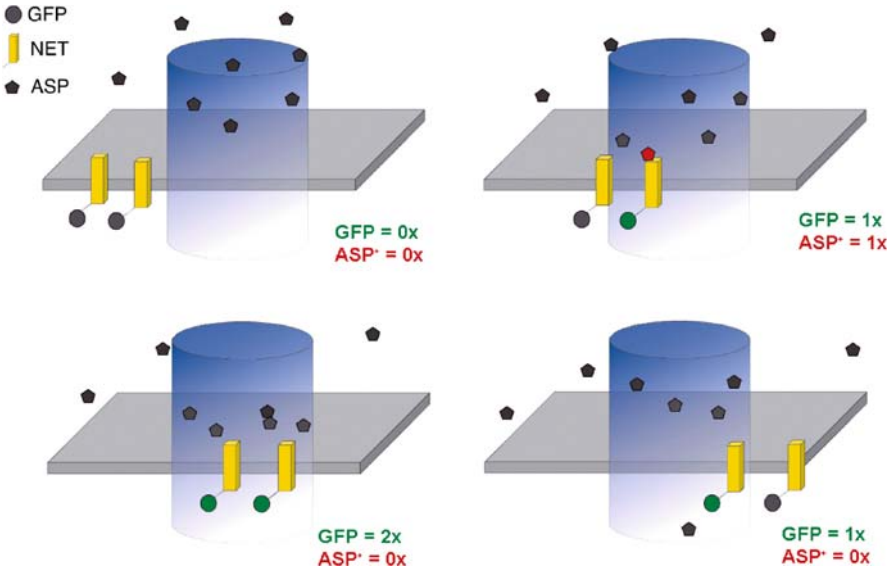

Fig. 9 Fluorescence correlation spectroscopy analyzes the fluorescence fluctuation due to diffusion or enzyme kinetics within a defined optical volume. Molecules outside the optical volume are not observed, thus do not contribute to the fluorescence signal. As fluorescent molecules diffuse into the optical volume, the signal increases. Molecules diffusing out of the optical volume have the opposite effect. The average fluorescence signal is proportional to the particle number, and the fluctuations provide a measure of diffusion time

state in which photoexcitation is not permitted. Under these conditions, the fluorescence intensity decreases although the particle remains in the optical volume. The resulting fluctuations are analyzed for autocorrelation.

$$G(\tau) = \langle F(t) \cdot F(t+\tau) \rangle \,/\, \langle F(t)^2 \rangle \tag{10}$$

The normalized autocorrelation function, $G(\tau)$, is calculated as the time average of the product of the fluctuations of the detected fluorescence $[F(t)]$ at every time t, and the fluctuations at the delayed times $t + \tau$, normalized by the average of the fluorescence emission $[F(t)]$. The zero time correlation ($\tau = 0$) is then $G(0) = F(t)^2/F(t)^2$. The temporal variation of $F(t)$ is proportional to $N(t)$, the fluctuations of the number of fluorophores in the probe volume. Since this is a shot-noise-limited measurement, $N(t)$ is sqrt(N), so $G(0)$ is proportional to $N(t)/N(t)2 = 1/N$, where N is the average number of fluorescent molecules in the probe volume.

The general autocorrelation function measures sustained self-similarity. $F(t)$ describes the original time-resolved data. $F(t + \tau)$ describes the translated data by the constant, τ. $F(t)^2$ is the average ensemble average. The resulting fluctuation can be analyzed in many ways, but the most common approach is by autocorrelation. Autocorrelation is a measure for the self-similarity of

a time signal. The original fluorescence signal is translated in time by adding a set amount (~10 μs) to each time point, without adjusting the corresponding fluorescence intensity. The resultant translated signal is compared to the original signal for correlation. The original signal is translated by an increased time (20 μs). The translated and original signals are compared for correlation. The process is iterated for increasing time intervals. Deviations in similarity provide characteristic time constants of underlying processes (Bacia and Schwille 2003; Dittrich et al. 2001; Haustein and Schwille 2003; Medina and Schwille 2002; Schwille 2001).

The autocorrelation is fit to a theory derived for the underlying fluctuations, thus experimental condition has an appropriate fit for the autocorrelation function. For example, a fluorescent molecule in solution is fit to a three-dimensional free diffusion model in which the molecule exits and enters the focal volume from any direction. If the molecule undergoes a transition from a dark to the light state, the fluctuations are observed in the autocorrelation. Multiplying the two independent fluctuation theories derives the resultant theory. The experimental condition mandates the autocorrelation theory applied.

$$G(\tau) = \frac{1}{N}\left(\frac{1 - F_B + F_B e^{-\tau/\tau_B}}{1 - F_B}\right)\left(\sum_{i=1}^{n} \frac{f_i}{\left(1 + \tau/\tau_{Di}\right)\sqrt{1 + \tau/\omega^2\tau_{Di}}}\right) \tag{10}$$

The autocorrelation function is derived for a three-dimensional diffusion model for an open system (Bacia and Schwille 2003). N is the average particle number. τ_D is the diffusion time of the particle in microseconds. ω is the axial ratio (ratio of axial to radial dimension of the observed volume). In each case, the observed fluctuations are dependent on the number of particles, N, and the diffusion of those particles in the observation volume. Membrane proteins are often fit to a two-dimensional diffusion model, because the protein movement is restricted to a single plane (Schwille et al. 1999). Schwille and coworkers (Bacia and Schwille 2003; Dittrich et al. 2001; Haustein and Schwille 2003; Medina and Schwille 2002; Schwille 2001) provide a detailed derivation of the autocorrelation function.

Prior to confocal and TPE microscopy, large focal volumes generated by a wide-field microscope required extremely dilute bright samples to minimize particle number. The fluorescent signal from large-particle numbers within the observation volume (Fig. 9) is not dramatically affected by the diffusion of a few particles. FCS sensitivity is inversely related to particle number; thus, low particle concentrations are ideal for FCS analysis. TPE microscopy and ultra-sensitive PMTs dramatically increased sensitivity and reduced particle numbers (Fig. 9), providing enhanced FCS measurements. Using a similar principle, cross-correlation analysis determines the relative similarity between two independent fluorescent signals. These data can provide a measure of association rates and protein–protein interactions or protein–ligand association. Multiple excitation lasers generate two different observation volumes, so dual

channel fluorescence cross-correlation spectroscopy (FCCS) requires normalization of these volumes. Calibrations with known diffusion times are used to determine the relative observation volume sizes (Bacia and Schwille 2003).

In summary, FCS provides fast time resolution and the ability to calculate the number of particles independent of local environment. FCS measures events ranging from 10 μs to 1 s, thus providing estimates of chemical kinetics, diffusion, and concentration. A major disadvantage to FCS is the need for low particle numbers. Although the confocal volume can limit the observation volume size, the number of particles must remain low (<50 particles). Also, FCS cannot distinguish single fluorescent molecules from a pair of joined fluorescent molecules. FCS requires a fivefold increase in particle diffusion to segregate distinct particles (Chen et al. 2002; Chen et al. 1999); thus, FCS analysis cannot distinguish a monomeric protein from a dimeric protein.

To investigate the kinetic relationship between ASP^+ and NET, we used FCS to determine the ASP^+ and NET concentration and mobility. Dual-channel FCS simultaneously measures GFP-hNET and ASP^+ fluctuations. Bath ASP^+ demonstrates diminished fluorescence ($\tau_{water} < 10$ ps) compared to cellular ASP^+ ($\tau_{cells} = 1.2$ ns), which permits the identification of bound ASP^+ (versus free ASP^+). Solution ASP^+ did not contribute to the total fluorescence signal. The autocorrelation function of ASP^+ intensity fluctuations reveals an ASP^+ transporter dwell time of 526±25 μs, which is significantly different from the relaxation time for GFP-hNET measured in the same optical volume (~0.15 fl, see Sect. 1.2). Analysis of GFP-tagged transporters gives a relaxation time of 30.2 ± 0.94 ms ($D = 0.17$ μm^2/s), which represents characteristically slow diffusion for a membrane protein (Meissner and Haberlein 2003; Vrljic et al. 2002). We also observe a 320-μs diffusion time, which correlated to known pH-dependent inter-conversion for GFP (Haupts et al. 1998); thus, FCS measurements are useful as a pH sensor for slow moving GFPs. The $\tau = 0$ intercept predicts the average particle (transporter) number per optical volume (Schwille 2001), thus providing a check on the FLIM calibration. The $G(0)$ autocorrelation values give 26 ± 0.98 (bound) ASP^+ particles and 26 ± 0.5 GFP-hNET (bound and free) particles in the optical volume, and the one-to-one ratio agrees with FLIM calculated ratio. We observe no cross-correlation between ASP^+ and GFP-hNET.

1.2.9 Fluorescence Recovery After Photobleaching

To corroborate the FCS diffusion measurements, we assessed hNET-GFP movement with FRAP. The methodologies presented above attempt to reduce photodamage to acquire a signal with high fidelity; however, FRAP experiments rely on photodegradation to measure fluorescent molecule kinetics. FRAP experimentation is often applied to study the movement of membrane proteins using a GFP-tagged conjugate protein. Under these conditions, a subsection within

an image is exposed to a high-intensity laser pulse. Only molecules within the subregion are photodegraded; thus, they appear dark after acquiring an image of the entire field. The recovery of the bleach region is related to the diffusion of the particle of interest. Like FCS, the recorded data are fit to a defined model to evaluate recovery. Siggia and coworkers (Siggia et al. 2000) describe a plausible model for membrane proteins.

GFP-hNET diffusion FRAP measurements provided similar kinetics to the FCS experimentation. Three pre-bleach GFP-hNET cell images were acquired prior to photodegradation of GFP-hNETs in a 4 μm by 18 μm region along the cell surface. Due to the geometry of HEK-293 cells (Fig. 10), we imaged the GFP-hNET cells along the membrane adjacent to the coverslip. HEK-293 cells form flat elongated surfaces adjacent to the membrane, permitting the idealized location for FRAP experiments. GFP-hNET was photodegraded using 100% laser intensity (~30 mW), followed by minimal exposure (<1 mW) to monitor the recovery. The damaged area recovers after approximately 1 min. These data were subsequently fit to an inhomogeneous diffusion model (Siggia

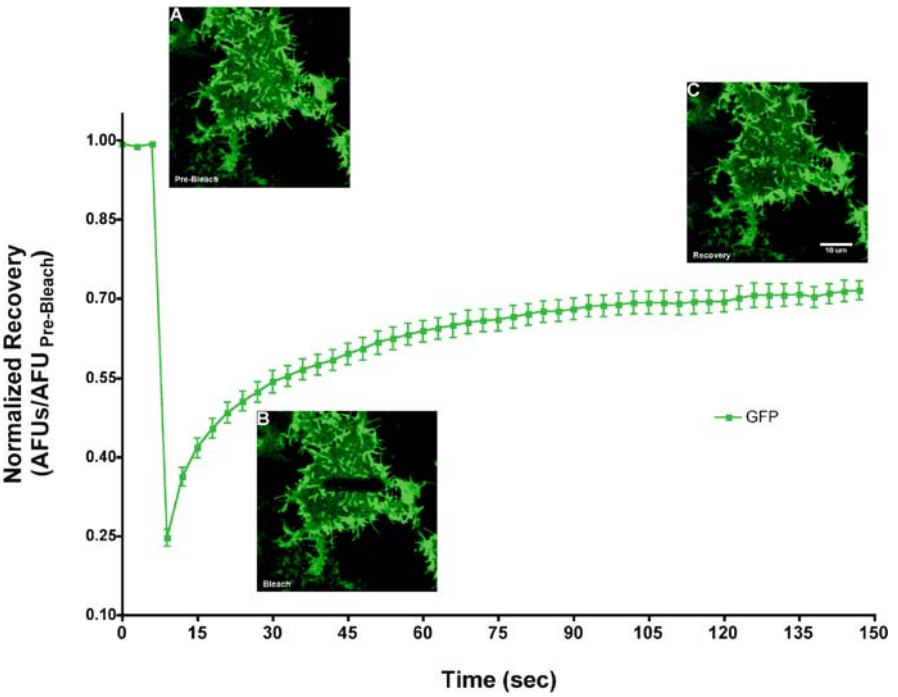

Fig. 10 FRAP measurements predict that GFP-hNET cells diffuse at 0.20 $\mu m^2/s$. GFP-hNET cells were imaged prior to photobleach (*inset A*) using a 40 × 1.3 NA lens at 4 × digital zoom. A 4-by-18 μm region was bleached from the cell membrane (*inset B*) from the membrane adjacent to the coverslip. After approximately 1 min the bleached region recovered (*inset C*). The time course for GFP-hNET recover provides a diffusion constant of 0.20 $\mu m^2/s$

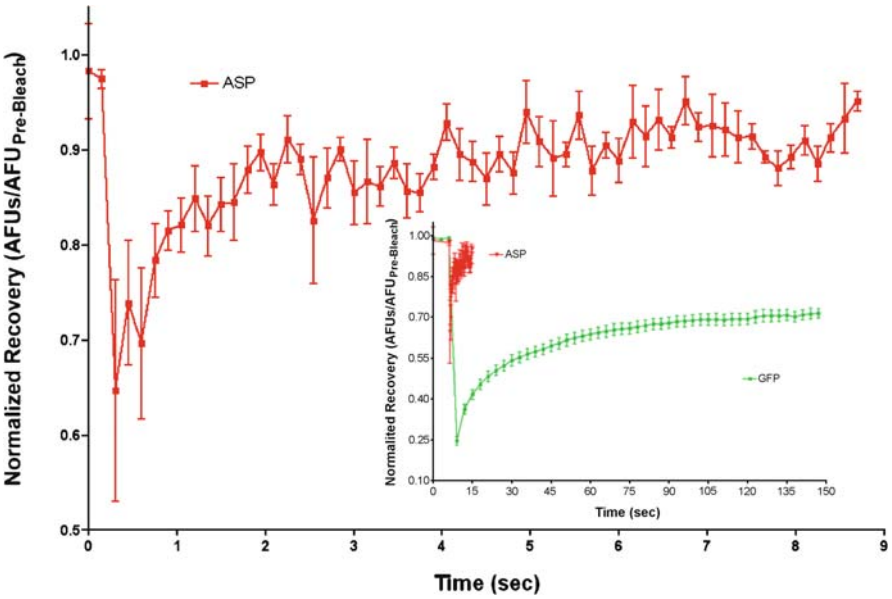

Fig. 11 FRAP experimentation cannot measure ASP^+ association rates. hNET-293 cells are exposed to 2 μM ASP^+. Several pre-bleach images were acquired prior to high-intensity light exposure. Several images were acquired, and ASP^+ recovered within 1 s. The *inset* shows the GFP-hNET and ASP^+ recoveries

et al. 2000) that yields an effective diffusion constant of 0.11 ± 0.3 $\mu m^2/s$ (Fig. 10). These data agree with the FCS-established diffusion times. Similar experimentation was performed using ASP^+ photobleach in hNET-293 cells, but the fluorescence recovered faster than the acquisition rate (Fig. 11); thus, these data cannot report an accurate rate measurement. The ASP^+ recovery was significantly faster than the GFP-hNET recovery (inset Fig. 11).

1.2.10 Fluorescence Plate Reader

The techniques described above are useful to measure single molecule properties. ASP^+ also has utility for large-volume high-information screening. The fluorescence-based assay described is amenable to a high-throughput screen via a fluorescence plate reader. Using a molecular devices flex station, Mason and coworkers monitored ASP^+ accumulation in cells expressing NET and DAT. The flex station excites a large volume (compared to confocal microscopy); thus, solution with ASP^+ significantly contributes to the total signal. Solution fluorescence is quenched with trypan blue enhancing the signal-to-noise for the automated assay. The plate reader accurately predicted IC_{50} values for inhibitors, such as DS and GBR-1206. These data indicate that this method can be

used to screen for other transporter inhibitors. According to the data presented, the fluorescence plate reader cannot distinguish binding from transport, which may be attributed to problem with ASP^+ administration.

2 Summary

This review outlines fluorescence methods used to measure absolute molecular concentrations, kinetic interactions of substrates and transporters, and diffusion constants of transporters in the membrane. The advantage of fluorescence methods, as opposed to classical biochemical methods, is that molecules are evaluated within a cellular context. Furthermore, fluorescence-based technologies are amenable to experiments on single molecules using high-throughput screening.

To alleviate the constraints associated with radiometric and other methods, we have used quantitative fluorescence microscopy to monitor dynamically the binding and transport of a fluorescent monoamine transporter substrate. Cells expressing monoamine transporters demonstrated an immediate increase in membrane-localized fluorescence following fluorescent substrate (ASP^+) application. After continued ASP^+ exposure (>30 s), the cell interior continued to increase in fluorescence. Although HEK-293 cells have non-monoamine transporter-mediated ASP^+ accumulation, at concentrations below 5 μM ASP^+ does not bind to parental HEK-293 plasma membranes. The nonspecific intracellular ASP^+ accumulation is one-tenth that of NET-expressing cells. The immediate ASP^+ increase, only seen in transfected cells, was composed of immobile ASP^+ molecules, which were displaced by subsequent antagonist (DS) administration. The slower accumulation inside the cell was arrested, but not displaced, by DS. These data indicate that ASP^+ initially binds to surface NETs and is subsequently transported. Known blockers or substrates (DS, cocaine, Na^+ or Cl^- substitution, and NE) each inhibited substrate binding and accumulation.

Confocal microscopy and TPE define optically isolated subvolumes within a large sample, thus providing "microscope cuvettes." Compartmentalized microscope cuvettes are digitally combined to produce a three-dimensional representation. FLIM provides a concentration-independent measurement to evaluate the local environment within the subvolume. In combination with confocal or TPE microscopy, FLIM establishes molecule concentrations. The established change in quantum yield allows a solution calibration curve that is corrected for environmental changes. FCS measures the diffusion time, concentration, and molecular brightness. In combination, these methods describe a molecular description of subcellular environments and molecular interactions.

Specific subcellular makers colocalized bound ASP^+ with the plasma membrane, and accumulated ASP^+ is associated with mitochondria. Optical isolation was accomplished by examining plasma membrane localized ASP^+ with

TIRF microscopy. The FLIM data showed that ASP^+ is highly sensitive to the local environment. The ASP^+ "fluorescence lifecycle" in our assay is as follows: ASP^+ is quenched by the aqueous solution until bound to NETs. After transport, the aqueous cytosolic environment again quenches ASP^+. ASP^+ subsequently associates with mitochondria, regaining optical activity. Although ASP^+ demonstrates significant environmental quantum yield changes, FLIM images provide the necessary conversion for solution ASP^+ to calibrate cellular ASP^+. ASP^+ is quenched in aqueous environments, such as the cytosol and is optically silent until bound to mitochondria. Calibrated confocal microscopy cannot measure the cytosolic pool, however, which requires complementary methods. Liquid chromatography tandem mass spectroscopy (LC/MS/MS) is employed to measure total ASP^+ accumulation (both dark and bright). These data indicated that mitochondrial ASP comprises only one-fifth the total accumulated ASP^+ at the time point measured. Thus, ASP^+ is less effective as a measure of uptake than it is of binding. This molecular conversion permits the assessment of pharmacological properties, such as surface density, transport velocity, and substrate-to-NET gene product stoichiometry.

FCS and FRAP experimentation provides information about substrate dwell time and transport motion in the plasma membrane. Due to the change in fluorescence lifetime, the fluctuations observed in FCS measurement of ASP^+ estimates the substrate dwell time on NET. Under identical conditions, we observed the relatively slow NET diffusion. The plasma membrane diffusion was substantiated by FRAP experimentation. These data may be substantiated and expanded by the application of image correlation spectroscopy (ICS) and photon-counting histogram (PCH). These methods are complimentary to the presented material, but have not been applied to ASP-bound NETs.

In summary, we have developed a calibrated microfluorometric assay that uniquely visualizes substrate binding and accumulation on single mammalian cells (or groups of cells) in real-time and which is amenable to high-throughput screening. In this review, we have used ASP-bound NETs as an example for multiple quantitative fluorescence microscopes, but these methods are applicable to other biological samples, such as receptor–ligand binding. These new approaches in microscopic fluorometry permit a more complete description and understanding of the underlying membrane protein biology.

Acknowledgements Supported by National Institutes of Health NS-34075.

References

Alcala JR, Gratton E, Jameson DM (1985) A multifrequency phase fluorometer using the harmonic content of a mode-locked laser. Anal Instrum 14:225–250

Axelrod D (1989) Total internal reflection fluorescence microscopy. Methods Cell Biol 30:245–270

Axelrod D (2001a) Selective imaging of surface fluorescence with very high aperture microscope objectives. J Biomed Opt 6:6–13
Axelrod D (2001b) Total internal reflection fluorescence microscopy in cell biology. Traffic 2:764–774
Axelrod D (2003) Total internal reflection fluorescence microscopy in cell biology. Methods Enzymol 361:1–33
Axelrod D, Thompson NL, Burghardt TP (1983) Total internal inflection fluorescent microscopy. J Microsc 129:19–28
Axelrod J, Kopin IJ (1969) The uptake, storage, release and metabolism of noradrenaline in sympathetic nerves. Prog Brain Res 31:21–32
Bacia K, Schwille P (2003) A dynamic view of cellular processes by in vivo fluorescence auto- and cross-correlation spectroscopy. Methods 29:74–85
Backs J, Haunstetter A, Gerber SH, Metz J, Borst MM, Strasser RH, Kubler W, Haass M (2001) The neuronal norepinephrine transporter in experimental heart failure: evidence for a posttranscriptional downregulation. J Mol Cell Cardiol 33:461–472
Batchelor M, Schenk JO (1998) Protein kinase A activity may kinetically upregulate the striatal transporter for dopamine. J Neurosci 18:10304–10309
Bauman PA, Blakely RD (2002) Determinants within the C-terminus of the human norepinephrine transporter dictate transporter trafficking, stability, and activity. Arch Biochem Biophys 404:80–91
Berland KM, So PT, Gratton E (1995) Two-photon fluorescence correlation spectroscopy: method and application to the intracellular environment. Biophys J 68:694–701
Blakely RD (1992) Molecular cloning and characterization of neurotransmitter transporters. NIDA Res Monogr 126:66–83
Blakely RD (2001) Physiological genomics of antidepressant targets: keeping the periphery in mind. J Neurosci 21:8319–8323
Blakely RD, Berson HE, Fremeau RT Jr, Caron MG, Peek MM, Prince HK, Bradley CC (1991) Cloning and expression of a functional serotonin transporter from rat brain. Nature 354:66–70
Bonisch H, Harder R (1986) Binding of 3H-desipramine to the neuronal noradrenaline carrier of rat phaeochromocytoma cells (PC-12 cells). Naunyn Schmiedebergs Arch Pharmacol 334:403–411
Bonisch H, Fuchs G, Graefe KH (1986) Sodium-dependence of the saturability of carrier-mediated noradrenaline efflux from noradrenergic neurones in the rat vas deferens. Naunyn Schmiedebergs Arch Pharmacol 332:131–134
Bradley CC, Blakely RD (1997) Alternative splicing of the human serotonin transporter gene. J Neurochem 69:1356–1367
Bruns D, Engert F, Lux HD (1993) A fast activating presynaptic reuptake current during serotonergic transmission in identified neurons of Hirudo. Neuron 10:559–572
Chen Y, Muller JD, So PT, Gratton E (1999) The photon counting histogram in fluorescence fluctuation spectroscopy. Biophys J 77:553–567
Chen Y, Muller JD, Ruan Q, Gratton E (2002) Molecular brightness characterization of EGFP in vivo by fluorescence fluctuation spectroscopy. Biophys J 82:133–144
Clark MS, Russo AF (1998) Measurement of tryptophan hydroxylase mRNA levels by competitive RT-PCR. Brain Res Brain Res Protoc 2:273–285
Corey JL, Quick MW, Davidson N, Lester HA, Guastella J (1994) A cocaine-sensitive Drosophila serotonin transporter: cloning, expression, and electrophysiological characterization. Proc Natl Acad Sci U S A 91:1188–1192

Dickinson ME, Simbuerger E, Zimmermann B, Waters CW, Fraser SE (2003) Multiphoton excitation spectra in biological samples. J Biomed Opt 8:329–338

Dittrich P, Malvezzi-Campeggi F, Jahnz M, Schwille P (2001) Accessing molecular dynamics in cells by fluorescence correlation spectroscopy. Biol Chem 382:491–494

Earles C, Schenk JO (1999) Multisubtrate mechanism for the inward transport of dopamine by the human dopamine transporter expressed in HEK cells and its inhibition by cocaine. Synapse 33:230–238

Elson EL, Magde D, Webb WW (1974) Fluorescence correlation spectroscopy. II. An experimental realization. Biopolymers 13:1–27

Foote S, Aston-Jones G (1995) Pharmacology and physiology of central noradrenergic systems. In: Bloom FE, Kupfer DJ (eds) Psychopharmacology: the fourth generation of progress. Raven Press, New York, pp 335–345

Foote SL, Aston-Jones G, Bloom FE (1980) Impulse activity of locus coeruleus neurons in awake rats and monkeys is a function of sensory stimulation and arousal. Proc Natl Acad Sci U S A 77:3033–3037

Galli A, DeFelice LJ, Duke BJ, Moore KR, Blakely RD (1995) Sodium-dependent norepinephrine-induced currents in norepinephrine-transporter-transfected HEK-293 cells blocked by cocaine and antidepressants. J Exp Biol 198:2197–2212

Galli A, Blakely RD, DeFelice LJ (1996) Norepinephrine transporters have channel modes of conduction. Proc Natl Acad Sci U S A 93:8671–8676

Galli A, Blakely RD, DeFelice LJ (1998) Patch-clamp and amperometric recordings from norepinephrine transporters: channel activity and voltage-dependent uptake [see comments]. Proc Natl Acad Sci U S A 95:13260–13265

Graefe KH, Bonisch H, Keller B (1978) Saturation kinetics of the adrenergic neurone uptake system in the perfused rabbit heart. A new method for determination of initial rates of amine uptake. Naunyn Schmiedebergs Arch Pharmacol 302:263–273

Gratton E, Jameson DM, Hall RD (1984) Multifrequency phase and modulation fluorometry. Annu Rev Biophys Bioeng 13:105–124

Hahn MK, Blakely RD (2002) Monoamine transporter gene structure and polymorphisms in relation to psychiatric and other complex disorders. Pharmacogenomics J 2:217–235

Hahn MK, Robertson D, Blakely RD (2003) A mutation in the human norepinephrine transporter gene (SLC6A2) associated with orthostatic intolerance disrupts surface expression of mutant and wild-type transporters. J Neurosci 23:4470–4478

Hanson KM, Behne MJ, Barry NP, Mauro TM, Gratton E, Clegg RM (2002) Two-photon fluorescence lifetime imaging of the skin stratum corneum pH gradient. Biophys J 83:1682–1690

Harder R, Bonisch H (1985) Effects of monovalent ions on the transport of noradrenaline across the plasma membrane of neuronal cells (PC-12 cells). J Neurochem 45:1154–1162

Haupts U, Maiti S, Schwille P, Webb WW (1998) Dynamics of fluorescence fluctuations in green fluorescent protein observed by fluorescence correlation spectroscopy. Proc Natl Acad Sci U S A 95:13573–13578

Haustein E, Schwille P (2003) Ultrasensitive investigations of biological systems by fluorescence correlation spectroscopy. Methods 29:153–166

Herman BD (2001) Fluorescence microscopy, 2nd edn. Bios Scientific Publishing, pp 1–170

Iversen LL, de Champlain J, Glowinski J, Axelrod J (1967) Uptake, storage and metabolism of norepinephrine in tissues of the developing rat. J Pharmacol Exp Ther 157:509–516

Jameson DM, Gratton E, Hall RD (1984) The measurement and analysis of heterogeneous emissions by multifrequency phase and modulation fluorometry. Appl Spectrosc Rev 20:55–106

Kitayama S, Ikeda T, Mitsuhata C, Sato T, Morita K, Dohi T (1999) Dominant negative isoform of rat norepinephrine transporter produced by alternative RNA splicing. J Biol Chem 274:10731–10736

Kitayama S, Morita K, Dohi T (2001) Functional characterization of the splicing variants of human norepinephrine transporter. Neurosci Lett 312:108–112

Lakowicz J (1999) Principles of fluorescence spectroscopy, 2nd edn. Kluwer Academic/ Plenum Publishers, New York, pp 368–394

Maes M, Lin AH, Verkerk R, Delmeire L, Van Gastel A, Van der PM, Scharpe S (1999) Serotonergic and noradrenergic markers of post-traumatic stress disorder with and without major depression. Neuropsychopharmacology 20:188–197

Magde D, Elson EL, Webb WW (1972) Thermodynamic fluctuations in a reacting system-measurement by fluorescence correlation spectroscopy. Phys Rev Lett 29:705–708

Magde D, Elson EL, Webb WW (1974) Fluorescence correlation spectroscopy. II. An experimental realization. Biopolymers 13:29–61

Mager S, Min C, Henry DJ, Chavkin C, Hoffman BJ, Davidson N, Lester HA (1994) Conducting states of a mammalian serotonin transporter. Neuron 12:845–859

Medina MA, Schwille P (2002) Fluorescence correlation spectroscopy for the detection and study of single molecules in biology. Bioessays 24:758–764

Meissner O, Haberlein H (2003) Lateral mobility and specific binding to GABA(A) receptors on hippocampal neurons monitored by fluorescence correlation spectroscopy. Biochemistry 42:1667–1672

Merlet P, Benvenuti C, Moyse D, Pouillart F, Dubois-Rande JL, Duval AM, Loisance D, Castaigne A, Syrota A (1999) Prognostic value of MIBG imaging in idiopathic dilated cardiomyopathy [see comments]. J Nucl Med 40:917–923

Minsky M (1957) Microscopy apparatus. US Patent No. 3013467

Moron JA, Brockington A, Wise RA, Rocha BA, Hope BT (2002) Dopamine uptake through the norepinephrine transporter in brain regions with low levels of the dopamine transporter: evidence from knock-out mouse lines. J Neurosci 22:389–395

Nelson PJ, Rudnick G (1981) Anion-dependent sodium ion conductance of platelet plasma membranes. Biochemistry 20:4246–4249

Ni YG, Chen JG, Androutsellis-Theotokis A, Huang CJ, Moczydlowski E, Rudnick G (2001) A lithium-induced conformational change in serotonin transporter alters cocaine binding, ion conductance, and reactivity of Cys-109. J Biol Chem 276:30942–30947

Patterson GH, Knobel SM, Sharif WD, Kain SR, Piston DW (1997) Use of the green fluorescent protein and its mutants in quantitative fluorescence microscopy. Biophys J 73:2782–2790

Pawley JB (1995) Handbook of biological confocal microscopy, 2nd edn. Plenum Press, New York, pp 1–632

Petersen CI, DeFelice LJ (1999) Ionic interactions in the Drosophila serotonin transporter identify it as a serotonin channel. Nat Neurosci 2:605–610

Piston DW, Masters BR, Webb WW (1995) Three-dimensionally resolved NAD(P)H cellular metabolic redox imaging of the in situ cornea with two-photon excitation laser scanning microscopy. J Microsc 178:20–27

Povlock SL, Schenk JO (1997) A multisubstrate kinetic mechanism of dopamine transport in the nucleus accumbens and its inhibition by cocaine. J Neurochem 69:1093–1105

Ramsey IS, DeFelice LJ (2002) Serotonin transporter function and pharmacology are sensitive to expression level: evidence for an endogenous regulatory factor. J Biol Chem 277:14475–14482

Rigler R, Mets U, Widengren J, Kask P (1993) Fluorescence correlation spectroscopy with high count rate and low background: analysis of translational diffusion. Eur Biophys J 22:169–175

Ritz MC, Cone EJ, Kuhar MJ (1990) Cocaine inhibition of ligand binding at dopamine, norepinephrine and serotonin transporters: a structure-activity study. Life Sci 46:635–645

Robertson D, Flattem N, Tellioglu T, Carson R, Garland E, Shannon JR, Jordan J, Jacob G, Blakely RD, Biaggioni I (2001) Familial orthostatic tachycardia due to norepinephrine transporter deficiency. Ann N Y Acad Sci 940:527–543

Rudnick G, Nelson PJ (1978) Platelet 5-hydroxytryptamine transport, an electroneutral mechanism coupled to potassium. Biochemistry 17:4739–4742

Sacchetti G, Bernini M, Bianchetti A, Parini S, Invernizzi RW, Samanin R (1999) Studies on the acute and chronic effects of reboxetine on extracellular noradrenaline and other monoamines in the rat brain. Br J Pharmacol 128:1332–1338

Schenk JO (2002) The functioning neuronal transporter for dopamine: kinetic mechanisms and effects of amphetamines, cocaine and methylphenidate. Prog Drug Res 59:111–131

Schildkraut JJ, Gordon EK, Durell J (1965) Catecholamine metabolism in affective disorders. I. Normetanephrine and VMA excretion in depressed patients treated with imipramine. J Psychiatr Res 3:213–228

Scholze P, Norregaard L, Singer EA, Freissmuth M, Gether U, Sitte HH (2002) The role of zinc ions in reverse transport mediated by monoamine transporters. J Biol Chem 277:21505–21513

Schroeter S, Apparsundaram S, Wiley RG, Miner LH, Sesack SR, Blakely RD (2000) Immunolocalization of the cocaine and antidepressant-sensitive 1-norepinephrine transporter. J Comp Neurol 420:211–232

Schwartz JW, Blakely RD, DeFelice LJ (2003) Binding and transport in norepinephrine transporters. Real-time, spatially resolved analysis in single cells using a fluorescent substrate. J Biol Chem 278:9768–9777

Schwille P (2001) Fluorescence correlation spectroscopy and its potential for intracellular applications. Cell Biochem Biophys 34:383–408

Schwille P, Korlach J, Webb WW (1999) Fluorescence correlation spectroscopy with single-molecule sensitivity on cell and model membranes. Cytometry 36:176–182

Shannon JR, Flattem NL, Jordan J, Jacob G, Black BK, Biaggioni I, Blakely RD, Robertson D (2000) Orthostatic intolerance and tachycardia associated with norepinephrine-transporter deficiency. N Engl J Med 342:541–549

Siggia ED, Lippincott-Schwartz J, Bekiranov S (2000) Diffusion in inhomogeneous media: theory and simulations applied to whole cell photobleach recovery. Biophys J 79:1761–1770

Sitte HH, Huck S, Reither H, Boehm S, Singer EA, Pifl C (1998) Carrier-mediated release, transport rates, and charge transfer induced by amphetamine, tyramine, and dopamine in mammalian cells transfected with the human dopamine transporter. J Neurochem 71:1289–1297

Sitte HH, Scholze P, Schloss P, Pifl C, Singer EA (2000) Characterization of carrier-mediated efflux in human embryonic kidney 293 cells stably expressing the rat serotonin transporter: a superfusion study. J Neurochem 74:1317–1324

Sitte HH, Hiptmair B, Zwach J, Pifl C, Singer EA, Scholze P (2001) Quantitative analysis of inward and outward transport rates in cells stably expressing the cloned human serotonin transporter: inconsistencies with the hypothesis of facilitated exchange diffusion. Mol Pharmacol 59:1129–1137

Sonders MS, Zhu SJ, Zahniser NR, Kavanaugh MP, Amara SG (1997) Multiple ionic conductances of the human dopamine transporter: the actions of dopamine and psychostimulants. J Neurosci 17:960–974

Tatsumi M, Groshan K, Blakely RD, Richelson E (1997) Pharmacological profile of antidepressants and related compounds at human monoamine transporters. Eur J Pharmacol 340:249–258

Torres GE, Gainetdinov RR, Caron MG (2003) Plasma membrane monoamine transporters: structure, regulation and function. Nat Rev Neurosci 4:13–25

Valentino RJ, Foote SL, Aston-Jones G (1983) Corticotropin-releasing factor activates noradrenergic neurons of the locus coeruleus. Brain Res 270:363–367

Vrljic M, Nishimura SY, Brasselet S, Moerner WE, McConnell HM (2002) Translational diffusion of individual class II MHC membrane proteins in cells. Biophys J 83:2681–2692

Wang YM, Xu F, Gainetdinov RR, Caron MG (1999) Genetic approaches to studying norepinephrine function: knockout of the mouse norepinephrine transporter gene. Biol Psychiatry 46:1124–1130

Wayment H, Meiergerd SM, Schenk JO (1998) Relationships between the catechol substrate binding site and amphetamine, cocaine, and mazindol binding sites in a kinetic model of the striatal transporter of dopamine in vitro. J Neurochem 70:1941–1949

Williams RM, Piston DW, Webb WW (1994) Two-photon molecular excitation provides intrinsic 3-dimensional resolution for laser-based microscopy and microphotochemistry. Faseb J 8:804–813

Xu F, Gainetdinov RR, Wetsel WC, Jones SR, Bohn LM, Miller GW, Wang YM, Caron MG (2000) Mice lacking the norepinephrine transporter are supersensitive to psychostimulants. Nat Neurosci 3:465–471